Hindawi
Journal of Control Science and Engineering
Volume 2023, Article ID 9790134, 1 page
https://doi.org/10.1155/2023/9790134

Retraction

Retracted: Thermal Effect Monitoring System of Dry-Type Smoothing Reactor

Journal of Control Science and Engineering

Received 15 August 2023; Accepted 15 August 2023; Published 16 August 2023

This article has been retracted by Hindawi following an investigation undertaken by the publisher [1]. This investigation has uncovered evidence of one or more of the following indicators of systematic manipulation of the publication process:

(1) Discrepancies in scope

(2) Discrepancies in the description of the research reported

(3) Discrepancies between the availability of data and the research described

(4) Inappropriate citations

(5) Incoherent, meaningless and/or irrelevant content included in the article

(6) Peer-review manipulation

The presence of these indicators undermines our confidence in the integrity of the article's content and we cannot, therefore, vouch for its reliability. Please note that this notice is intended solely to alert readers that the content of this article is unreliable. We have not investigated whether authors were aware of or involved in the systematic manipulation of the publication process.

Wiley and Hindawi regrets that the usual quality checks did not identify these issues before publication and have since put additional measures in place to safeguard research integrity.

We wish to credit our own Research Integrity and Research Publishing teams and anonymous and named external researchers and research integrity experts for contributing to this investigation.

The corresponding author, as the representative of all authors, has been given the opportunity to register their agreement or disagreement to this retraction. We have kept a record of any response received.

References

[1] J. Hu, M. Shi, C. Jiao, and G. Zhu, "Thermal Effect Monitoring System of Dry-Type Smoothing Reactor," *Journal of Control Science and Engineering*, vol. 2022, Article ID 3040713, 8 pages, 2022.

Hindawi
Journal of Control Science and Engineering
Volume 2022, Article ID 3040713, 8 pages
https://doi.org/10.1155/2022/3040713

Research Article

Thermal Effect Monitoring System of Dry-Type Smoothing Reactor

Jingen Hu, Minglei Shi, Chenhua Jiao, and Guichi Zhu

EHV Branch Company of State Grid Zhejiang Electric Power Co., Ltd., Hangzhou, Zhejiang 310007, China

Correspondence should be addressed to Jingen Hu; 31115313@njau.edu.cn

Received 31 May 2022; Revised 26 June 2022; Accepted 2 July 2022; Published 20 July 2022

Academic Editor: Jackrit Suthakorn

In order to study the influence of harmonic current loss characteristics on the thermal effect of UHV dry smoothing reactor, the author proposes a thermal effect monitoring system under the loss mechanism of dry smoothing reactor. By adding the electromagnetic loss density to the temperature field as a heat source, the electromagnetic-thermal multiphysics mapping relationship is established, the convective heat transfer process is more accurately simulated, and the temperature rise calculation is realized. Finally, the temperature rise test of the dry-type smoothing reactor is carried out. Experimental results show that using the calculation method considering the characteristics of harmonic loss, the maximum error between the calculated value and the experimental value is 9.1%, the average error is 4.34%, and the temperature rise distribution law is in good agreement. The system meets the requirements of engineering precision and provides the corresponding theoretical basis for engineering designers.

1. Introduction

With the sustained and rapid growth of the national economy, the demand for electricity is increasing, and the scale of the power system continues to develop. However, the geographical distribution of energy resources and economic development in many local power grids is uneven .For example, a large amount of power installed in my country is located in the western hydropower base and the northern thermal power base. This requires the realization of power transmission from west to east, mutual supply between north and south, and national networking. The limitations of AC power transmission, such as the limitation of synchronous operation stability during long-distance power transmission, make DC power transmission technology re-emphasized. High-voltage direct current (HVDC) transmission is widely used in long-distance large-capacity transmission, power system networking, and submarine cable transmission [1].

The smoothing reactor, also known as the DC reactor, is one of the most important equipment for HVDC transmission, and is generally connected in series between the converter and the DC line. Its main functions are as follows: when a disturbance or accident occurs in the DC system, it can suppress the rising speed of the DC current to avoid the expansion of the accident; when the inverter fails, it can avoid commutation failure; when the AC voltage drops, the probability of inverter commutation failure can be reduced; when the DC line is short-circuited (Figure 1), the peak value of the short-circuit current can be limited with the cooperation of the regulator. Together with the DC filter, it can greatly suppress and reduce the harmonic voltage and harmonic current generated during the commutation process, thus greatly weakening the interference to communication along the DC line. At low DC load, avoid high overvoltage caused by inductive components such as converter transformers due to current interruption. Limit the discharge current of the line and capacitive equipment installed at the line end through the converter valve. According to the main differences in main insulation and magnetic circuit structure, smoothing reactors can be divided into two types: dry-type hollow core type and oil-immersed iron core type [2]. Both types of smoothing reactors have successful operating experience in HVDC transmission projects.

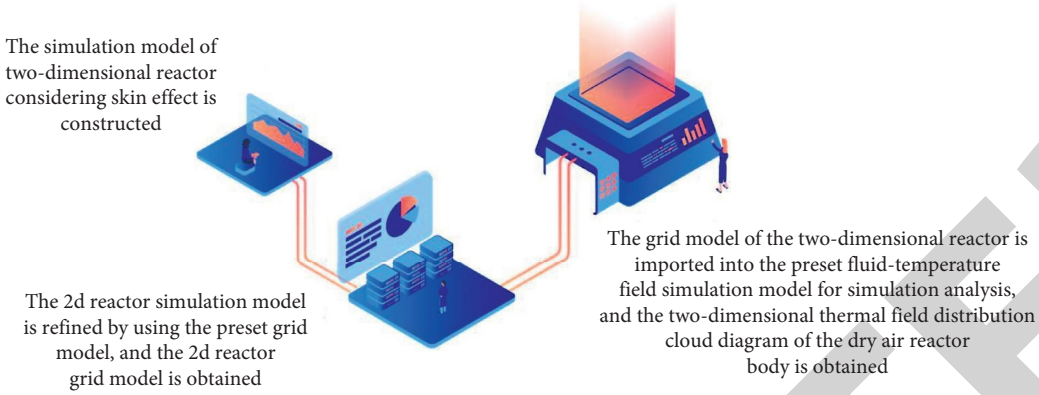

Figure 1: Thermal effect detection system.

2. Literature Review

Che-Galicia et al. based on some advantages of smoothing reactor inductance and existing operating experience, according to the preliminary plan of ±800 kV DC transmission project and the investigation of related manufacturers, comparing the economy and technology of the indoor and outdoor arrangement of the smoothing reactor, it is found that both indoor and outdoor arrangements are feasible [3]. Volkov et al. calculated that under the impact of lightning waves, turn-to-turn overvoltage of ±800 kV UHV DC dry-type smoothing reactor. Under the lightning impulse, the inter-turn voltage of the outer layer of the reactor is large, and the largest is the inter-turn overvoltage of the first turn of the outermost layer [4]. Xsa et al. successfully extended the analytical formula for the magnetic field of a single-turn toroidal wire to the analytical formula for the magnetic field of a solenoid coil using multiple integrals, confirming the feasibility of the superposition method [5]. Basinas and others used the superposition principle to calculate the magnetic field distribution of the reactor on the basis of the predecessors, and deduced the analytical formula of the magnetic induction intensity at any point in the magnetic field of the multilayer and parallel coils [6]. Dlj et al. tested the reactor to verify the effectiveness of the superposition calculation idea. Generally speaking, before using the analytical method to calculate the magnetic field of the reactor, it is necessary to know the physical parameters and geometric size data of the reactor (including the number of encapsulations, the number of turns, the width of the air passage, the thickness of the insulation of the turns, the wire diameter, the winding height, etc.), and then superimpose the magnetic field calculation formula of the dry-type air-core reactor with multilayer coils in parallel to the calculation of the magnetic field of the single-layer coil [7]. Evseev et al. take the idea of superposition as the core. The calculation program of the magnetic field distribution of the reactor is written, but due to the hollow structure of the reactor, the magnetic field is scattered in a wide area. If you want to calculate the reactor with a little more complicated parameters, the calculation amount will become very huge [8].

For the study of the temperature field of the dry-type smoothing reactor, the temperature rise test method specified in the national standard is mostly used in engineering, but the test conditions are relatively high. With the rise of multiphysics coupled numerical calculation, the research of coupled temperature field and fluid field has become a research hotspot. Gui et al. carried out the simulation calculation of the fluid-structure coupling temperature field of an ultra-high voltage dry-type smoothing reactor based on the finite volume method, analyzed the temperature rise distribution law, and used the optical fiber temperature measurement method to carry out the simulation calculation temperature rise test. This method is also a research hotspot in the current dry-type smoothing reactor temperature rise calculation [9].

The author considers the influence of harmonic current on the loss characteristics and uses the analytical calculation method and the finite element method to analyze the DC loss, AC loss, eddy current loss, and eddy current loss of the encapsulated winding in a dry-type smoothing reactor. Then, the required loss density is coupled to the three-dimensional temperature field to solve the temperature rise distribution. Finally, the temperature rise test is carried out to verify the rationality and accuracy of the calculation method.

3. Research Methods

3.1. Computational Model

3.1.1. Physical Model. The author takes an ultra-high voltage dry-type smoothing reactor of ±800 kV/6 250 A as an example, and establishes a physical model, which includes 26 layers of coaxial cylindrical wrapping windings and two upper and lower star frames. Nonresearch objects such as noise cover, support bar, connection accessories, insulating resin, etc. are ignored in the modeling [10]. At the same time, considering that the circular aluminum stranded wire inside the winding cannot be modeled finely, an equivalent model of the encapsulated winding is established.

3.1.2. Circuit Model. In HVDC transmission projects, the transmission of DC power needs to go through processes such as rectification and inversion, which will inevitably generate a small amount of harmonic current [11]. The

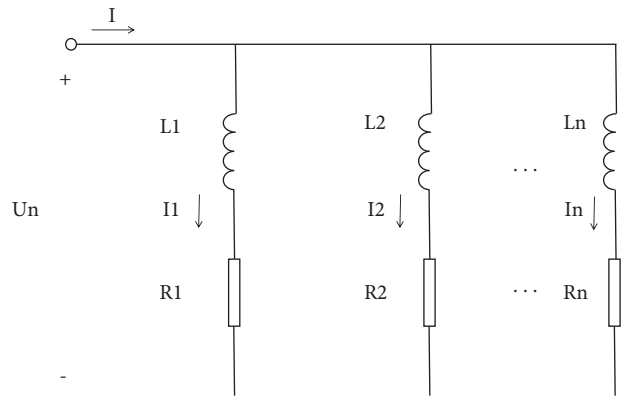

Figure 2: Equivalent circuit model.

encapsulated windings of each layer of the dry-type smoothing reactor adopt a coaxial parallel structure, and the total current is shunted to the windings of each layer through the bus bar. Therefore, it can be regarded as a circuit composed of 26 branches containing resistance and inductance in terms of electrical characteristics, as shown in Figure 2.

In Figure 2: U_n represents the voltage at both ends of the branch; I represents the total current; R_1, R_2. . ., R_n represent the resistance value of each layer of encapsulation; $M_{1,2}$, $M_{2,n}$, . . . etc. represent the mutual inductance between each layer of encapsulation; I_1, I_2, . . ., I_n represent the current flowing through each layer of encapsulation. The circuit model can be expressed as the following formula:

$$\left(\begin{bmatrix} R_1 & 0 & 0 \\ 0 & R_2 & 0 \\ \cdots & \cdots & \cdots \\ 0 & 0 & R_n \end{bmatrix} + j\omega \begin{bmatrix} L_1 & M_{1,2} & M_{1,n} \\ M_{2,1} & L_2 & M_{2,n} \\ \cdots & \cdots & \cdots \\ M_{n,1} & M_{n,2} & L_n \end{bmatrix}\right)\begin{bmatrix} I_1 \\ I_2 \\ \cdots \\ I_n \end{bmatrix} = \begin{bmatrix} U_1 \\ U_2 \\ \cdots \\ U_n \end{bmatrix}. \quad (1)$$

Formula (1) is simplified to the following formula:

$$(\mathbf{K}_R + j\omega\mathbf{K}_M)\mathbf{I} = \mathbf{U}. \quad (2)$$

In formula (2): $\mathbf{K}_R$ represents the resistance matrix, which is calculated by the definition formula of resistance; $\mathbf{K}_M$ represents the inductance matrix, which is calculated based on the finite element software; I represents the current matrix; U represents the voltage matrix.

By multiplying the inverse matrix $(\mathbf{K}_R + j\omega\mathbf{K}_M)^{-1}$ on both sides of equation (2), the current matrix can be obtained as in the following equation:

$$\mathbf{I} = (\mathbf{K}_R + j\omega\mathbf{K}_M)^{-1}U. \quad (3)$$

The current excitation in each envelope winding can be obtained by solving the current matrix I.

3.2. Loss Calculation Method Considering Higher Harmonics. The main structure of the dry-type smoothing reactor does not contain ferromagnetic materials. The encapsulation winding is made of multistrand parallel-wound circular aluminum stranded wires, and the star frame is made of aluminum alloy material [12].

Under actual working conditions, the current flowing through the dry-type smoothing reactor is mainly DC current and also includes harmonic current. Therefore, when the dry-type smoothing reactor is actually running, the loss of the encapsulated winding includes DC resistance loss, AC resistance loss, and eddy current loss.

Compared with DC current, the proportion of harmonic current is small, but due to the existence of high-frequency harmonic current, on the one hand, the alternating magnetic field will induce eddy current loss in the aluminum stranded wire inside the encapsulating winding; on the other hand, with the increase in frequency, the skin effect and proximity effect of harmonic currents in the conductors become more and more obvious, and the calculation of using DC resistance instead of AC resistance will cause certain errors [13]. The relationship between the DC resistance R_{dc} and the AC resistance R_{ac} of the encapsulated winding satisfies the following formula:

$$\begin{cases} R_{ac} = k_s R_{dc}, \\ k_s = 1 + \dfrac{(r_0/\delta_0)^4}{48 + 0.8(r_0/\delta_0)^4}, \\ \delta_0 = \dfrac{1}{\sqrt{\pi f \mu \gamma}}. \end{cases} \quad (4)$$

In formula (4): f is the harmonic frequency; γ is the electrical conductivity; μ is the magnetic permeability; r_0 is the wire radius.

Due to the constraints of computer capacity and mesh quantity, it is difficult to finely model the circular aluminum stranded wire inside the encapsulated winding in finite element calculation software, the author adopts the analytical method to calculate the electromagnetic loss of the encapsulated winding, in which the DC resistance loss and the AC resistance loss are calculated by the following equation:

$$P_{ri} = I_{dc}^2 R_{dc} + \sum_{n=1}^{50} I_n^2 R_{acn}. \quad (5)$$

In formula (5): P_{ri} represents the resistance loss of the ith layer of encapsulation windings; I_{dc} represents the DC current of the ith layer of encapsulation windings; I_n represents the nth harmonic current of the ith layer of encapsulation windings, up to the 50th order.

The eddy current loss of each layer of encapsulated winding can be inferred from the eddy current loss of a single wire. Since the diameter of a single round wire is much smaller than the overall size of the reactor, it can be approximately considered that its internal magnetic field is equal to the central magnetic field of the wire, at the same time, ignoring the eddy current magnetic interaction [14]. The formula for calculating the eddy current loss of a single round wire is as follows:

$$P_e = \sum_{n=1}^{50} \frac{\gamma\ D\omega_n^2\pi^2 d^4}{128} B_n^2. \quad (6)$$

In formula (6): P_e represents the eddy current loss of a single round wire; D represents the diameter of the enclosing winding where the wire is located; ω_n represents the angular frequency of the nth harmonic; B_n represents the maximum magnetic induction intensity at the center of the wire under the nth harmonic; d represents The diameter of the wire.

The loss density q_i of the encapsulated winding of the ith layer can be obtained from the following equation:

$$\begin{cases} P_i = P_{ri} + P_{ei}, \\ q_i = \dfrac{P_i}{V_i}. \end{cases} \quad (7)$$

In formula (7): P_i represents the total loss of the ith layer of encapsulation windings; P_{ei} represents the eddy current loss of the ith layer of encapsulation windings; V_i represents the volume of the ith layer of encapsulation windings [15].

The star frame is the main structural component in this model, and its loss is caused by the eddy current induced by the harmonic current magnetic field. The author introduces the magnetic vector potential A and the scalar potential φ based on Maxwell's equations and solves the star frame eddy current loss by the finite element method as in the following equation.

$$\begin{cases} \nabla \times \dfrac{1}{\mu} (\nabla \times A) = \sigma - (j\omega A - \nabla\varphi), \\ P_s = \displaystyle\int_{V_s} \frac{|J_e|^2}{\sigma} dV_s. \end{cases} \quad (8)$$

In formula (8): σ represents the conductivity; ω represents the angular frequency. In the right-hand term of the equation, $(-\sigma\nabla\varphi)$ represents the source current density J_s; $-j\omega A$ represents the induced eddy current density J_e due to the time-varying magnetic field.

3.2.1. Result Analysis. Based on the Ansys Maxwell magnetic field solver, the current load excitation obtained by equation (3) is added to the encapsulated windings of each layer simulate the magnetic field distribution of a dry smoothing reactor. The magnetic field distribution of the reactor is highly symmetrical, decreasing from the center to both sides and reaching a maximum value of 0.208 T near the center of the first layer of encapsulated windings. The equivalent heat source density of each layer of the dry-type smoothing reactor encapsulated winding is shown in Table 1.

Figure 3 shows the comparison results of the total loss calculated when the DC resistance loss is without considering the harmonic loss characteristics and considering the AC loss and eddy current loss. In Figure 3, the 5, 9, and 13 layers of the encapsulation winding AC loss and eddy current loss account for 5.1%, 6.9%, and 5.8% of the total loss, respectively.

Based on the eddy current field solver, the simulation and numerical calculation of the eddy current of the star-shaped dry-type smoothing reactor under the load operating condition are carried out. Among them, under the action of 100 Hz harmonic current, the maximum value of star-frame current density is 6.22×10^5 A/m^2. Affected by the space magnetic field, the distribution of eddy currents is less uniform. The eddy current density near the lower edge of the encapsulated winding is larger, showing a significant eddy current effect [16]. The calculated total eddy current loss of the star frame is about 875.6 W.

3.3. Calculation of Temperature Rise

3.3.1. Heat Transfer Mechanism. Due to the high symmetry of the physical model, the calculation model of the temperature field of the dry smoothing reactor can be simplified to 1/4 of the original model. The interior of the dry-type smoothing reactor adopts thermal conduction to transfer heat and dissipates heat with the surrounding air mainly through natural convection and thermal radiation [17].

The heat transfer equation for the encapsulated winding layer in the solution domain is as follows:

$$\frac{\partial}{\partial x}\left(k_x \frac{\partial T}{\partial x}\right) + \frac{\partial}{\partial y}\left(k_y \frac{\partial T}{\partial y}\right) + \frac{\partial}{\partial z}\left(k_z \frac{\partial T}{\partial z}\right) + q_i = \rho c \frac{\partial T}{\partial t}. \quad (9)$$

In formula (9): T represents the temperature of the solid; k_x, k_y, and k_z represent the thermal conductivity of the solid in the three-dimensional space , respectively; r represents the fluid density; c represents the specific heat capacity.

The gas enters from the vent below and flows out from above, and its flow satisfies the mass conservation equation, the energy conservation equation and the Navier-Stokes equation as the following equation:

$$\frac{\partial(\rho u)}{\partial x} + \frac{\partial(\rho v)}{\partial y} + \frac{\partial(\rho w)}{\partial z} = 0, \quad (10)$$

$$\mathrm{div}(\mathrm{UT}) = \mathrm{div}\left[\frac{\lambda}{\rho c}\mathrm{grad}T_f\right] + \frac{S_T}{\rho}, \quad (11)$$

$$\begin{cases} \mathrm{div}(\mathrm{uU}) = \mathrm{div}(\mathrm{vgradu}) - \dfrac{1}{\rho}\dfrac{\partial p}{\partial x}, \\ \mathrm{div}(\mathrm{vU}) = \mathrm{div}(\mathrm{vgradu}) - \dfrac{1}{\rho}\dfrac{\partial p}{\partial y}, \\ \mathrm{div}(\mathrm{wU}) = \mathrm{div}(\mathrm{vgradu}) - \dfrac{1}{\rho}\dfrac{\partial p}{\partial z}. \end{cases} \quad (12)$$

In formulas (10)–(12): u, v, w represent the components of velocity vector U in ; p represents fluid pressure; v represents fluid kinematic viscosity; I represents fluid thermal conductivity; S_T represents microfluidic source term.

3.3.2. Result Analysis. The electromagnetic loss density is coupled into the fluent temperature field as the initial heat source, and the temperature rise of the dry-type hollow

Table 1: Encapsulation equivalent heat source density.

Layers	/(W·m^{-3})	layers	/(W·m^{-3})
1	9712.97	14	17045.07
2	11881.01	15	17603.84
3	12683.68	16	17444.15
4	13297.38	17	17894.81
5	13374.27	18	18970.07
6	13524.25	19	19148.23
7	14170.03	20	19826.43
8	14602.68	21	20000.77
9	14987.75	22	20209.65
10	15766.01	23	20438.13
11	16616.52	24	20471.61
12	16858.96	25	20067.72
13	19712.97	26	19393.29

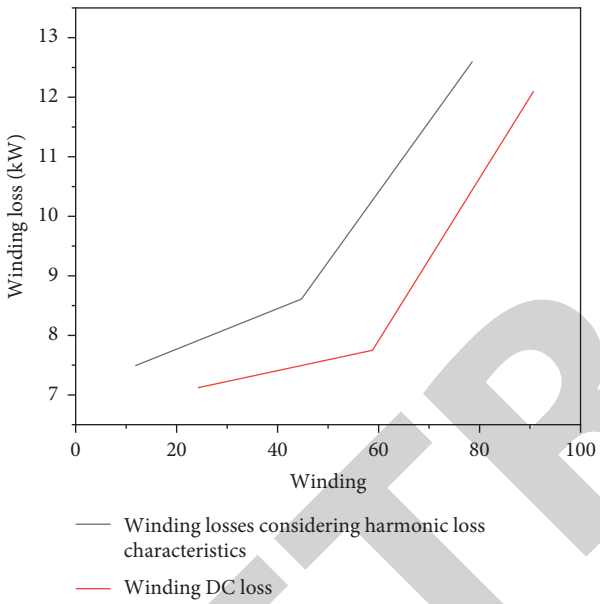

Figure 3: Comparison of DC resistance loss of an encapsulated winding and total loss considering harmonics.

smoothing reactor under natural ventilation is calculated. The encapsulated windings near the inside and outside have better heat dissipation conditions and lower temperatures, while the heat dissipation conditions of the inner encapsulated windings are poor, and the maximum temperature from the 13th layer to the upper end face of the 23rd layer exceeds 90°C.

After further postprocessing of each layer of encapsulation, it is judged that the highest temperature rise is located at the upper end face of the 17-layer encapsulated winding, showing that the maximum temperature rise is 62.8°C. The calculation results show that the temperature at the upper end of the encapsulation axis of each layer is the highest, followed by the temperature in the middle area and the lowest at the lower end. According to the theoretical analysis of heat transfer and fluid mechanics, it is concluded that in the process of convection heat dissipation, the viscosity of air increases with the increase of temperature, which is affected by its own viscosity and wall friction. After the gas at the bottom end absorbs a lot of heat, it rises under the action of natural convection, and the gas velocity gradually decreases at the cooling surface, forming a thin heat exchange layer [18]. The increase of the self-wall viscous force will increase the thickness of the heat exchange layer, which is not conducive to heat dissipation. Therefore, the temperature of the dry-type smoothing reactor on the axial height increases with the increase of the axial height.

The air velocity distribution of the cut plane is smaller at the inlet, and when the gas flows under the reactor, the velocity increases and enters the air passage between the encapsulated windings and takes away part of the heat. On the outer wall of the reactor, the gas flow rate is also higher. Finally, the maximum velocity at the exit is 1.398°m/s.

4. Analysis of Results

4.1. Test Method. In order to verify the rationality and accuracy of the calculation method, a temperature rise test was carried out in accordance with the national standard. Since it is difficult to directly load harmonic current, according to the loss equivalent principle in the national standard, the harmonic current is converted to DC current as the following equation:

$$I = \sqrt{\frac{I_d^2 \times R_{dc} + \sum_{n=1}^{50} I_n^2 \times R_{acn}}{R_{dc}}}. \quad (13)$$

In formula (13): I represents the applied equivalent temperature rise test current; I_d represents the direct current; I_n represents the nth harmonic current.

4.2. Test Results and Comparison. During the test, the temperature measurement system was selected using a low-light temperature-taking wire clip temperature measurement system.

The principle of the temperature measurement system of the low-light electric wire clip is to use the low-light electric temperature sensor fixed on the wire. It is transmitted to the data transmission base station in real time by wireless, and the data transmission base station sends the collected data information to the monitoring center in real time through the GPRS wireless communication network. It enables the line operation and maintenance department to grasp the heating situation and temperature development trend data in time. According to this parameter, the operation and maintenance department can carry out scientific and dynamic expansion. In order to further upgrade the transmission efficiency of power transmission lines, the products can work stably under high electromagnetic fields and a wide temperature range of −40°C to +125°C [19]. Using low-power design, wireless isolation, radio frequency communication, low-light power acquisition and other technologies, it has the characteristics of complete isolation, convenient installation, strong anti-interference ability, reliable and continuous operation, etc., and it can well solve the temperature measurement problem under high-voltage state [20]. The collected temperature is communicated

through radio frequency in real time, transmission to the host for uninterrupted and accurate measurements.

The temperature monitoring sensors are distributed at each monitoring point of the wire clip, which measures the surface temperature of the wire clip in real time and sends the temperature data to the data transmission base station wirelessly. The data transmission base station is composed of large-capacity batteries, solar panels, controllers, and data transmission relays. The batteries, solar panels, and controllers provide power to the data transmission relays. After the data transmission relay receives the sensor data, the data is transmitted to the power system server in an encrypted way through 4G [21]. The background display terminal of the centralized control center can check the real-time temperature and historical curve of each sensor at any time. If there is an over-temperature situation, it can quickly locate and notify the relevant personnel in time [22].

The measured temperature distribution of the dry-type smoothing reactor increases from bottom to top, and the temperature is the highest at the upper end face, and the trend is consistent with the simulation results [23].

The comparison between the final measurement results of the temperature rise test and the simulation calculation values is shown in Figures 4 and 5. It can be seen from Figure 4 that there are 15 layers in the 26-layer encapsulation. The error between the experimental measurement value and the simulation calculation value is less than 5%. It can be seen from Figure 5 that the calculated values of layers 1 to 10 and layers 24 to 26 are lower than the experimental values. The reason for the error is the simplification of the noise cover by the simulation model, resulting in higher heat dissipation conditions than the actual ones. The experimental measured values at the 17th to 23rd floors are slightly lower than the calculated values, which may be due to the neglect of the effects of ventilation and heat dissipation of structures such as airway braces and rain cover. After calculation, the error between the simulation calculation value and the test value is controlled within 9.1%, and the average error is 4.34%, which meets the requirements of engineering accuracy [24].

4.3. Performance Analysis. The design performance of the UHV dry-type smoothing reactor requires that in outdoor use, the average temperature rise does not exceed 65°C under the action of long-term temperature rise test current and harmonic equivalent current, and the temperature rise of the hot spot does not exceed 85°C. The average temperature rise obtained from the test is 58.1°C, and the hot spot temperature rise is 63.9°C, which meets the design requirements [25].

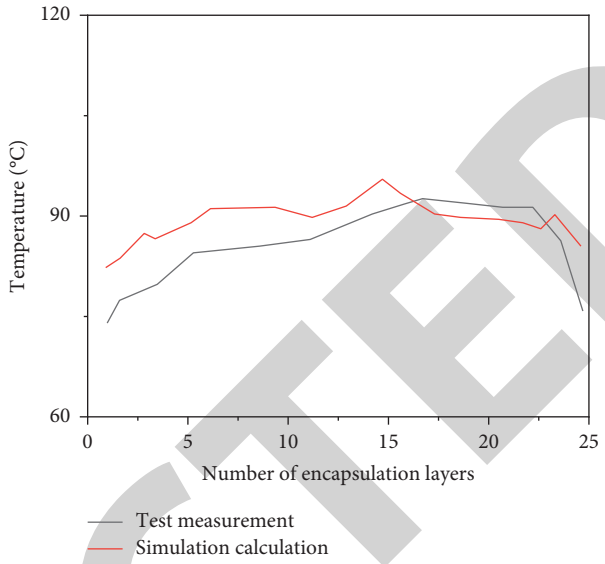

Figure 4: Temperature comparison of the reactor.

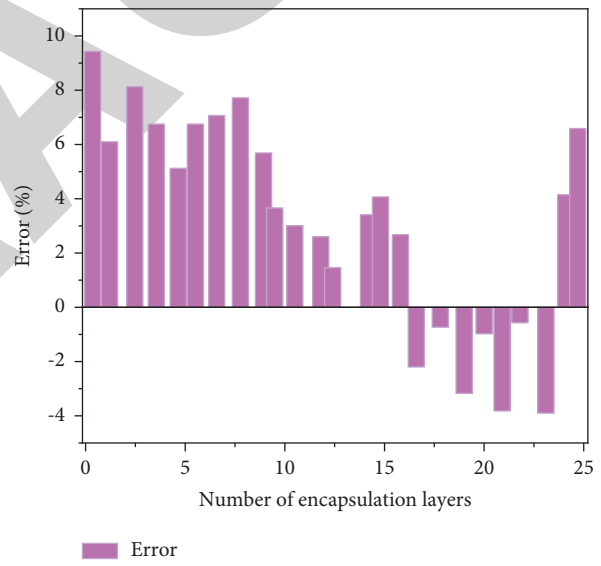

Figure 5: Comparison of the temperature error of the reactor.

5. Conclusion

The author puts forward a calculation method of the dry-type smoothing reactor considering the characteristics of harmonic loss, calculating the electromagnetic loss of a ±800°kV/625 A dry-type smoothing reactor and solves the distribution of its electromagnetic field and temperature field. The thermal effect was simulated and verified by the temperature rise test, and finally the following conclusions were drawn:

(1) When calculating the electromagnetic loss of a dry smoothing reactor, the influence of harmonic current on electromagnetic loss cannot be ignored. The calculation of the eddy current loss and AC resistance loss of the encapsulated winding needs to use the analytical method, and the calculation of the eddy current loss of the structural parts needs to use the finite element method.

(2) The distribution law of the magnetic field and temperature field of the reactor is summarized and analyzed. The magnetic field distribution is highly symmetrical, decreasing from the center to both sides, and the magnetic induction intensity reaches its maximum value near the center of the first layer of encapsulated windings. The temperature rise distribution shows an increasing trend in the axial direction, and the temperature gradually increases from the bottom to the top.

(3) Considering the calculation method of harmonic loss characteristics, the error between the simulation calculation value and the test value is controlled within 9.1%, and the average error is 4.34%, which meets the requirements of engineering accuracy and verifies the rationality of this calculation method.

Conflicts of Interest

The authors declare that there are no conflicts of interest.

Acknowledgments

Fund Project: Science and technology project of State Grid Zhejiang Electric Power Co., Ltd. Projece No: 5211mr20004u.

References

[1] T. K. Koca and M. Y. Koca, "Variations in ultrasonic wave velocities of miocene carbonate and clastic sedimentary rocks under dry and fully water saturated conditions," *Environmental Earth Sciences*, vol. 80, no. 3, pp. 1–20, 2021.

[2] J. Yang, Z. He, Z. Zhang, Y. Liu, and M. Yin, "Propagation characteristics of pressure wave in cylindrical reactor induced by underwater pulsed arc discharge," *IEEE Transactions on Plasma Science*, vol. 3, no. 99, pp. 1–9, 2021.

[3] G. Che-Galicia, H. A. Váquiro-Herrera, L. Sampieri, and E. Corona-Jiménez, "Ultrasound-assisted extraction of phenolic compounds from avocado leaves (persea americana mill. var. drymifolia): optimization and modeling," *International Journal of Chemical Reactor Engineering*, vol. 18, no. 7, pp. 2192–2205, 2020.

[4] V. Y. Volkov, L. A. Goliborodo, A. A. Krutikov, and O. V. Kudryavtsev, "Modeling of thermohydraulic processes in a steam generator with several plugged heat-transfer tubes," *Thermal Engineering*, vol. 69, no. 2, pp. 77–86, 2022.

[5] B. Xsa, B. Xz, B. Fwa, B. Lya, D. Yan, and S. A. Yong, "Thermochemical analysis of dry methane reforming hydrogen production in biomimetic venous hierarchical porous structure solar reactor for improving energy storage - sciencedirect," *International Journal of Hydrogen Energy*, vol. 46, no. 11, pp. 7733–7744, 2021.

[6] P. Basinas, J. Rusín, and K. Chamrádová, "Dry anaerobic digestion of the fine particle fraction of mechanically-sorted organic fraction of municipal solid waste in laboratory and pilot reactor," *Waste Management*, vol. 136, pp. 83–92, 2021.

[7] A. Dlj, B. Jlla, A. Ap, and C. Bla, "Methane dry reforming over ni/al 2 o 3 catalyst in spark plasma reactor: linking computational fluid dynamics (cfd) with reaction kinetic modelling," *Catalysis Today*, vol. 362, pp. 11–21, 2021.

[8] A. M. Evseev, V. N. Meshcheryakov, and A. I. Boikov, "Electric-power-quality characteristics of industrial dc electric-arc facilities," *Russian Electrical Engineering*, vol. 92, no. 12, pp. 772–777, 2022.

[9] G. Gui, N. J. Brooks, H. C. Kapteyn, M. M. Murnane, and C. T. Liao, "Second-harmonic generation and the conservation of spatiotemporal orbital angular momentum of light," *Nature Photonics*, vol. 15, 2021.

[10] B. Yue, N. Mei, P. Xu et al., "Quantitative analysis of ac/dc side harmonic transfer characteristics for modular multilevel converter and suppression measures," *IEEE Access*, vol. 8, 2020.

[11] Y. Li, Y. Yang, S. Sima, B. Li, X. Sun, and X. Li, "Non-intrusive load monitoring based on harmonic characteristics," *Procedia Computer Science*, vol. 183, no. 7, 2021.

[12] C. Fang, H. Wu, L. Cao, Y. Li, and J. Miao, "Modified least-squares finite element method for solving the Boltzmann transport equation with spherical harmonic angular approximation," *Annals of Nuclear Energy*, vol. 140, 2020.

[13] B. Wang, S. Dong, F. Liu, and J. Hu, "A simple equivalent temperature rise test method suitable for safely evaluating thermal limits of motors and power devices without model dependence," *IEEE Transactions on Industrial Electronics*, vol. 67, no. 10, pp. 8755–8766, 2020.

[14] A. S. Saragih, A. E. Putra, and R. Dhelika, "The experiment of thickness relationship on ceramic fiberboard and silicon carbide to temperature rise in microwave oven for sintering hydroxyapatite," *Key Engineering Materials*, vol. 833, pp. 209–213, 2020.

[15] H. S. Dhami, P. R. Panda, D. P. Mohanty, and K. Viswanathan, "An analytical method for predicting temperature rise due to multi-body thermal interaction in deformation processing," *Journal of Occupational Medicine*, vol. 74, no. 2, pp. 513–525, 2022.

[16] S. H. Jin and K. Y. Jung, "Effect of calcination temperature and ti substitution on optical properties of (fe,cr)2o3 cool black pigment prepared by spray pyrolysis," *RSC Advances*, vol. 12, no. 1, pp. 72–77, 2021.

[17] S. Zhao, J. Dong, C. Lv, Z. Li, W. Sun, and W. Zhang, "Thermal mismatch effect and high-temperature tensile performance simulation of hybrid CMC and superalloy bolted joint by progressive damage analysis," *International Journal of Aerospace Engineering*, vol. 2020, no. 2, Article ID 8739638, 2020.

[18] Q. Min, E. P. Li, J. M. Jin, and W. Chen, "Electrical–thermal cosimulation of coaxial TSVs with temperature-dependent mos effect using equivalent circuit models," *IEEE Transactions on Electromagnetic Compatibility*, vol. 3, no. 99, pp. 1–10, 2020.

[19] C. Li, P. Ge, and W. Bi, "Thermal simulation of the single discharge for electro-spark deposition diamond wire saw," *International Journal of Advanced Manufacturing Technology*, vol. 114, 2021.

[20] X. Zhao, B. Fu, W. Zhang et al., "Increasing the thermal conductivity of styrene butadiene rubber: insights from molecular dynamics simulation," *RSC Advances*, vol. 10, no. 39, 2020.

[21] M. Fan and A. Sharma, "Design and implementation of construction cost prediction model based on SVM and LSSVM in industries 4.0," *International Journal of Intelligent Computing and Cybernetics*, vol. 1, 2021.

[22] S. Shriram, J. Jaya, S. Shankar, P. Ajay, and B. Nagaraj, "Deep learning-based real-time AI virtual mouse system using computer vision to avoid COVID-19 spread," *Journal of Healthcare Engineering*, vol. 2021, Article ID 8133076, 2021.

[23] J. Hu, Y. M. Kang, Y. H. Chen, X. Liu, and Q. Liu, "Analysis of aerosol optical depth variation characteristics for 10 years in Urumqi based on MODIS_c006," *Huan Jing Ke Xue*, vol. 39, no. 8, pp. 3563–3570, 2018.

[24] R. Huang, S. Zhang, W. Zhang, and X. Yang, "Progress of zinc oxide-based nanocomposites in the textile industry," *IET Collaborative Intelligent Manufacturing*, vol. 3, pp. 281–289, 2021.

[25] E. Guo, V. Jagota, M. Makhatha, and P. Kumar, "Study on fault identification of mechanical dynamic nonlinear transmission system," *Nonlinear Engineering*, vol. 10, no. 1, pp. 518–525, 2021.